Rare Met. (2014) 33(5):499–510
DOI 10.1007/s12598-014-0398-9

RARE METALS
www.editorialmanager.com/rmet

Research progress in Mg-based hydrogen storage alloys

Dong-Liang Zhao*, Yang-Huan Zhang

Received: 9 September 2014 / Revised: 12 September 2014 / Accepted: 15 September 2014 / Published online: 4 October 2014

Abstract Magnesium and magnesium-based alloy hydrides remain attractive hydrogen storage materials owing to high hydrogen capacity and rich reserves in the earth's crust. A high stability of hydride and sluggish hydriding/dehydriding kinetics at practical temperatures for the materials drove researchers into alloying with other elements, using different preparation techniques, using catalyst and thin film hydride to improve the hydrogen absorption/desorption properties. In this review, the development of these approaches and their effects on the thermodynamic and kinetics properties of magnesium and magnesium-based alloy hydrides were descript in details.

keywords Magnesium-based storage alloy; Thermodynamic and kinetics; Preparation technique; Alloying and catalyzing

1 Introduction

New-type hydrogen storage alloy with high capacity is the key to promote the application of fuel cell [1]. Of the many options for the candidate's storing hydrogen alloys, magnesium and magnesium-based alloys increasingly attract much attention due to their abundance, low density, and high amount of hydrogen storage. The content of hydrogen absorption for MgH_2, Mg_2NiH_4, Mg_2FeH_6, and Mg_2RENiH_7 are 7.6 wt%, 3.6 wt%, 4.5 wt%, 5.4 wt%, and 6.5 wt% under certain temperature and pressure of hydrogen, respectively [2–6]. Although Mg-based alloy with crystalline structure has higher hydrogen storage capacity, their poor hydrogen absorption/desorption kinetics resulting from the extremely high thermodynamics stability of metal hydride limit their practical application. In order to break through these obstacles, various approaches, including alloying with other elements, adding catalysts using mechanical milling, and thin film material, were adopted and important progresses were achieved. This paper presents a summary on the recent advances and developments on Mg and Mg-based materials.

D.-L. Zhao*, Y.-H. Zhang
Department of Functional Material Research, Central Iron and Steel Research Institute, Beijing 100081, China
e-mail: dlzhao@sina.com

2 Alloying with transition metal and rare earths

Generally, the method of rare earth elements, transition metal, or combination substituting for Mg is confirmed to effectively decrease the desorption temperature and remove other thermodynamic constrains of Mg and Mg-based alloys. One reason is that Mg and transition metals (Ni, Cu, Co, Fe, Mn, etc.) form alloy such as Mg_2Ni, Mg_2Cu, Mg_2Co, Mg_2Fe, and Mg_3Mn binary alloys. Despite the lower hydrogen storage capacity of the alloys compared with that of the MgH_2, it has much faster hydrogen absorption and desorption kinetics. Another reason is that RE hydrides involving (La, Ce, Nd, Sm)-H can form during hydrogen absorption process and catalyze the hydrogen sorption and releasing reactions in the alloys, thus improving the hydrogenating and dehydrogenating kinetics of Mg hydride. Consequently, it is believed that alloying of Mg with transition metals, REs, and combination is beneficial to exhibit outstanding hydrogen storage properties of Mg and Mg-based hydrogen storage alloy.

Multiphase structure involving composition of Mg-M, RE-Mg, and RE-Mg-M easily form after partial substitution for Mg with combinations of metals and REs, which facilitates the

improvement of thermodynamic and kinetic properties during hydrogen absorption and desorption reaction.

Hu and Ren et al. [7, 8] reported that $LaMg_2Cu$ alloy containing $LaMg_2Cu_2$ and $LaMg_3$ phases and $LaMg_2Ni_{1.67}$ alloy containing La_2Mg_{17}, $LaMg_3$, and Mg_2Ni phases could exhibit excellent absorption and desorption kinetics because of abundant phase interfaces as hydrogen diffusion channels and buffer areas for releasing distortion and stress of the crystal lattice in the alloys. Liu et al. [9] found that the $LaMg_{8.40}Ni_{2.34-x}Al_x$ ($x = 0$, 0.20) alloys were composed of La_2Mg_{17}, $LaMg_2Ni$, and Mg_2Ni phases. The substitution for Ni with Al could not change the alloy phase. However, the phase distribution of $LaMg_{8.40}Ni_{2.14}Al_{0.20}$ alloy was much more uniform compared with that of $LaMg_{8.40}Ni_{2.34}$ alloy. The reversible hydrogen storage capacity of $LaMg_{8.40}Ni_{2.14}Al_{0.20}$ was 3.22 wt% at 558 K, higher than the value of 3.01 wt% of $LaMg_{8.40}Ni_{2.34}$ alloy. In addition, the Mg hydride in $LaMg_{8.40}Ni_{2.14}Al_{0.20}$ alloy was less stable than that in $LaMg_{8.40}Ni_{2.34}$ alloy, which was ascribed to the fact that Mg hydride was transformed from the reaction of La_2Mg_{17} with hydrogen in the activation process and the Al element could solute in the La_2Mg_{17} phase. $LaMg_{8.40}Ni_{2.14}Al_{0.20}$ alloy also shows faster hydriding and dehydriding kinetics. So it was believed that the partial substitution for Ni with Al could effectively enhance the hydrogen storage capacity and improve the kinetic performance of magnesium and transition metal-based alloys.

Pei et al. [10] added four rare earths (La, Ce, Pr, and Nd) to Mg_2Ni alloy and found that the composition of $REMg_2Ni$ alloys is formed. A single-phase composition of $REMg_2Ni$ phase was found when RE was one of three elements (La, Pr, and Nd), and a double-phase composition of $CeMg_2Ni$ and $CeMg_3$ phases when RE was Ce. In the process of the hydrogen absorption, $REMg_2Ni$ phases transform to rare earth hydrides (RE-H) and Mg_2NiH_4 phase, and for $CeMg_3$ phase, it was decomposed to $CeH_{2.74}$ and MgH_2 phases. The RE-H played an important role in improving hydrogen storage properties of Mg_2Ni phase in RMg_2Ni alloys. The enthalpy change in the hydrogen absorption and desorption process of Mg_2Ni phase in $REMg_2Ni$ alloys was smaller than that of pristine Mg_2Ni alloy, which indicated that the RE-H could reduce the enthalpy of the Mg_2Ni phase. Meanwhile, RE-H could accelerate the hydriding rate of Mg_2Ni phase. The uptake time for the hydrogen content reaching 90 % of their maximum hydrogen storage capacity was shorter than that of pristine Mg_2Ni alloy. At 573 K, the $NdMg_2Ni$ alloy had the highest hydrogen storage capacity and dehydriding plateau, and the descending order of hysteresis was $PrMg_2Ni < NdMg_2Ni < CeMg_2Ni < LaMg_2Ni$ (Table 1, [10]), which suggested that the $PrMg_2Ni$ alloy exhibited a better cycling stability and reversibility than the other three alloys. At 523 K, the uptake time of $REMg_2Ni$ (RE = La, Ce, Pr, and Nd) alloys reaching 90 % of the maximum hydrogen storage capacity was 75, 34, 65, and 52 s for La, Ce, Pr, and Nd, respectively, which were much shorter than 110 s of pristine Mg_2Ni alloy. The RE-H in the alloys not only improved their thermodynamic properties but also accelerated their hydriding kinetics. Pei et al. [11] also investigated the phase structure and hydrogen storage property of $LaMg_{3.93}Ni_{0.21}$ alloy. X-ray diffraction (XRD) and scanning electron microscope (SEM) results exhibited that $LaMg_{3.93}Ni_{0.21}$ alloy consisted mainly of $LaMg_3$, La_2Mg_{17}, and $LaMg_2Ni$ phases; after hydriding/dehydriding process, all the three phases transformed, La_3H_7 phase existed, and the actual hydrogen absorption phases were Mg and Mg_2Ni phases. The reversible hydrogen storage capacity of $LaMg_{3.93}Ni_{0.21}$ alloy was 2.63 wt%, and the absorption time reaching 90 % of the storage capacity was 124 s at 523 K, and that was 1850 s for deabsorbing 90 % of the maximum dehydrogen capacity. The hydriding process of $LaMg_{3.93}Ni_{0.21}$ alloy followed the nucleation and growth mechanisms. The enthalpy and entropy for hydriding and dehydriding reactions of the Mg phase in $LaMg_{3.93}Ni_{0.21}$ alloy were calculated to be (-66.38 ± 1.10) $kJ \cdot mol^{-1}$, (-100.96 ± 1.96) $J \cdot K \cdot mol^{-1}$ and (68.50 ± 3.87) $kJ \cdot mol^{-1}$, (98.28 ± 5.48) $J \cdot K \cdot mol^{-1}$, respectively. A comparison of these data with those of MgH_2 (-74.50 $kJ \cdot mol^{-1}$, -132.30 $J \cdot K \cdot mol^{-1}$) suggested that the hydride of $LaMg_{3.93}Ni_{0.21}$ alloy was less stable than MgH_2. The existence of La hydride and synergetic effect of multiphase led to higher reversible hydrogen storage capacity and better kinetic property at lower temperature for $LaMg_{3.93}Ni_{0.21}$ alloy.

Xie et al. [12] reported that substitution for Mg with Nd in Mg_2Ni alloy promoted the appearance of multiphase structure involving Mg_2Ni, Nd_2Ni_7, $NdMg_{12}$, or Nd_5Mg_{41} and other minor phases in the $Mg_{2-x}Nd_xNi$ ($x = 0$, 0.1, 0.2, 0.3) alloys. The addition of Nd transformed the phase of the alloys. In $Mg_{1.9}Nd_{0.1}Ni$ alloy, the main phase was Mg_2Ni, and there was a small quantity of some binary alloy phases such as Nd_5Mg_{41}, Nd_2Ni_7, and $NdMg_{12}$; while in $Mg_{1.8}Nd_{0.2}Ni$ and $Mg_{1.7}Nd_{0.3}Ni$ alloy, the main phases became Mg_2Ni and Nd_2Ni_7, and the contents of Nd_5Mg_{41}

Table 1 Hydrogen storage properties of $REMg_2Ni$ (RE = La, Ce, Pr, and Nd) alloys at 573 K

Alloys	Hydrogen storage capacity/wt%	Hydriding plateau/MPa	Dehydriding plateau/MPa	Hysteresis
$LaMg_2Ni$	1.92	0.2443	0.1205	0.701
$CeMg_2Ni$	1.78	0.3617	0.1884	0.652
$PrMg_2Ni$	1.84	0.3241	0.2005	0.480
$NdMg_2Ni$	2.07	0.3269	0.2021	0.491

and $NdMg_{12}$ increased correspondingly. The alloys could be activated within only one hydrogen absorption and desorption cycle. The substitution for Mg with Nd improved the hydrogen storage properties of Mg_2Ni evidently and kept relative high hydrogen capacities. The pressure composition temperature (PCT) of the Mg–Nd–Ni alloys displayed two plateaus, the lower and narrower ones corresponding to MgH_2 formation and the higher and broader ones corresponding to Mg_2NiH_4 formation. Among the Mg–Nd–Ni alloys, the hydrogen absorption kinetics was enhanced significantly and the alloys kept a relative high hydrogen storage capacity. Except for $Mg_{1.9}Nd_{0.1}Ni$, the desorption kinetics of $Mg_{1.7}Nd_{0.3}Ni$ and $Mg_{1.8}Nd_{0.2}Ni$ were deteriorated compared with Mg_2Ni. The $Mg_{1.9}Nd_{0.1}Ni$ alloy exhibited the best hydrogen absorption and desorption kinetics, and the hydrogen capacities were 3.47 wt% and 3.50 wt% at 573 and 623 K, respectively.

Binary and ternary Mg-based alloys with Fe, Al, and Ti as alloying elements were studied [13]. The dehydrogenation kinetics binary $Mg_{70}Al_{30}$ and $Mg_{75}Ti_{25}$ alloys decreased after several cycles due to alloying of the Ta and Pd catalyst layers or decomposition of a metastable ternary hydride phase. In binary $Mg_{70}Fe_{30}$, Mg_2FeH_6 could form, but was not reversible at 200 °C. The ternary alloys showed superior performance over the binary ones. This was most likely due to their multiphase structure; the interphase areas of both Mg phase and Ti–Al or Ti–Fe phases provided good pathways for hydrogen diffusion and surface catalysts. Kinetically, the $Mg_{70}Al_{15}Ti_{15}$ and $Mg_{70}Fe_{15}Ti_{15}$ showed the best performance, fully desorbing their total capacity of approximately 4 wt% within 15 min, which remained stable for over 100 cycles. The Mg–Al–Fe alloys, which did not form a hydride-forming secondary phase, performed considerably worse, although the presence of Al made Mg_2FeH_6 phase in $Mg_{70}Al_{10}Fe_{20}$. Of all the compositions tested, $Mg_{85}Al_{7.5}Ti_{7.5}$ had the highest reversible capacity of 5.4 wt% and performed kinetically only slightly worse than $Mg_{70}Al_{15}Ti_{15}$.

Ren et al. [8] investigated the structure of the as-cast and quenched $Mg_{20-x}La_xNi_{10}$ ($x = 0, 2, 4, 6$) alloys; for convenience, the alloys were denoted with La content as La_0, La_2, La_4, and La_6, respectively. There was no amorphous phase in the as-quenched Mg_2Ni alloy, but the as-quenched alloys ($x \geq 2$) presented a feature of the nanocrystalline alloy embedded in the amorphous matrix, confirming that the substitution for Mg with La significantly enhanced the glass-forming ability of the $Mg_{20-x}La_xNi_{10}$ ($x = 0, 2, 4, 6$) hydrogen storage alloys. La substitution ($x = 2$) did not change the major phase of the as-cast alloy, but with La content further rising, the major phase of the as-cast alloys changed from Mg_2Ni into (La, Mg) Ni_3 + $LaMg_3$ phase (Fig. 1, [8]). The substitution for Mg with La markedly

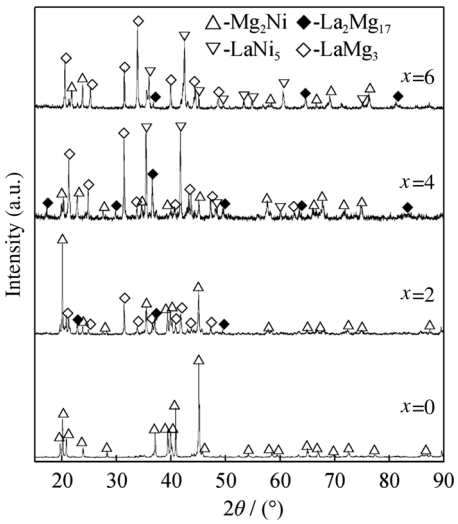

Fig. 1 XRD patterns of as-cast $Mg_{20-x}La_xNi_{10}$ ($x = 0$–6) alloys

increased the hydrogen absorption and desorption capacities and the kinetics of the as-cast $Mg_{20-x}La_xNi_{10}$ ($x = 0$, 2, 4, 6) alloys. The as-quenched alloy ($x = 2$) displayed the maximum hydrogen desorption capacity and excellent kinetics, but with La content further increasing, the hydrogen absorption and desorption capacities of the as-quenched alloys significantly declined, owing to the change of the major phase in the alloys caused by La substitution. The substitution for Mg with La clearly increased the discharge capacity of the as-cast alloys. The discharge capacities of the as-quenched alloys had the maximum values with the variation of La content. The cycle stability of the as-cast and quenched alloys was significantly improved with La content increasing (Fig. 2, [8]), which was ascribed to the increase of the glass-forming ability and the change of the major phase of the alloy caused by La substitution.

Knotek and VoJtěch [14] prepared eighteen as-cast binary Mg–Ni, Mg–Mm, and ternary Mg–Ni–Mm and Mg–Ni–TM (TM = transition metals Cu, Zn, Mn, and Co; Mm = mischmetal containing Ce, La, Nd, and Pr) alloys and determined the alloys with the most potential for electrochemical hydrogen storage. These alloys had fine eutectic structure composed of α-Mg and intermetallic phase rich in elements, such as Ni, Co, and RE, which had good catalytic effect on hydriding. In terms of hydrogen surface concentration and hydrogen penetration depth, the best hydriding performance was observed for the Mg–26Ni alloy with a purely eutectic structure. However, regarding the total mass of hydrogen absorbed during electrochemical hydriding, the Mg–25Ni–12Mm alloy had the best performance. In this alloy, catalytic activities of both Ni and Mm were combined, and the Mm addition also changed the hydriding mechanism and facilitated the inward

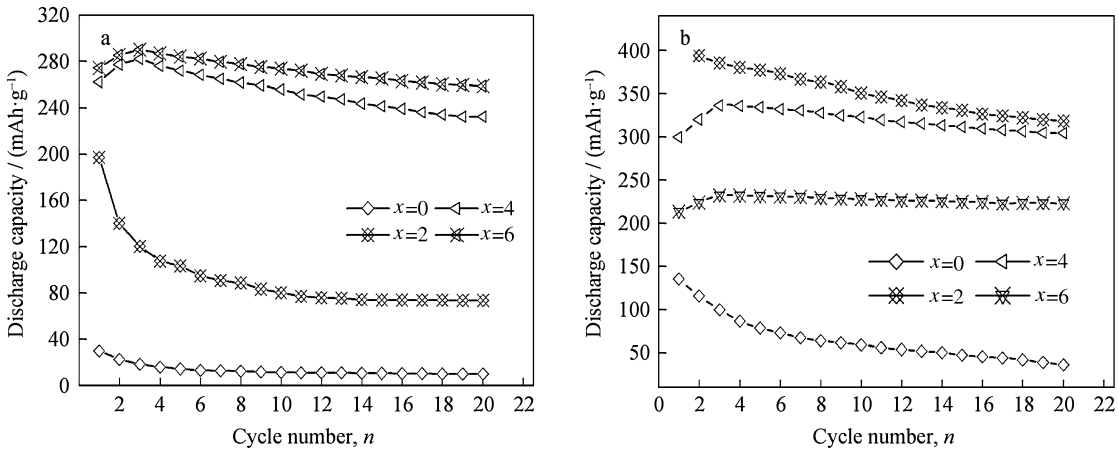

Fig. 2 Evolution of discharge capacity of $Mg_{20-x}La_xNi_{10}$ alloys with cycle number: **a** as-cast and **b** as-quenched (20 $m \cdot s^{-1}$)

diffusion of hydrogen. Both the Mg–26Ni and Mg–25Ni–12Mm alloys were prospective materials for electrochemical storage of hydrogen because the main hydriding product of these alloys was the binary MgH_2 hydride which can theoretically absorb 7.6 wt% hydrogen. The maximum hydrogen concentrations of 1.6 wt% and 1.0 wt% reached were seemingly low, but it should be taken into account that the studied alloys were in the as-cast state.

3 Improving surface and kinetics properties by preparation technique

Ultra-particle, micro- and nano-crystalline, or amorphous structure of Mg and Mg-based alloys could be obtained by ball milling, rapid solidification, and other techniques. Nano-sized Mg particle exhibits several advantages: (1) increased surface area Mg reacting with hydrogen, (2) shortened hydrogen diffusion distances, and (3) increased number of atoms at grain boundaries and interfaces to enhance the hydrogen diffusion rates. Theoretical studies predicted that thermodynamic properties of MgH_2 would be significantly improved when the MgH_2 nanoparticle size was reduced to smaller than 2.0 nm [15–20].

Poletaev et al. [21] found that thin ribbons with composition of $LaMg_{12}$ were produced by solidifying the melt on a spinning copper wheel in an argon atmosphere using three different rotations speeds: 3.1, 10.5, and 20.9 $m \cdot s^{-1}$. The phase structure and microstructure of the alloys were closely related to the solidification rate. There are three types of the parent crystal structures in La–Mg alloys, including the firstly reported hexagonal $TbCu_7$ type in the paper and the earlier tetragonal $ThMn_{12}$ and orthorhombic $LaMg_{11}$ types. A metastable $TbCu_7$-type structure was firstly known for the La–Mg system. From the scanning electron microscopy (SEM) studies, rapid solidification was found to cause a significant grain refinement and an amorphization for the highest cooling rate (Fig. 3, [21]).

The particle size of the formed hydride phases varied in the range of 0.2–3.0 μm depending on the rapid solidification synthesis route used to prepare the original alloy. Hydrogen absorption resulted in a two-step disproportionation process:

$$LaMg_{12} + H_2 \rightarrow LaH_3 + Mg \rightarrow LaH_3 + MgH_2 \quad (1)$$

A decrease in the grain size improved the hydrogenation kinetics. Hydrogen desorption studied by thermal desorption spectroscopy (TDS) and in situ synchrotron radiation X-ray diffraction (SR XRD) showed a major peak of hydrogen evolution at 370 °C. For the alloys synthesized at 10.5 and 20.9 $m \cdot s^{-1}$, it was accompanied by an extra desorption event at 415 °C. This extra peak was associated with Mg-assisted low-temperature hydrogen desorption from LaH_2 proceeding below 450 °C, leading to a recombination process to form the initial intermetallic alloy $LaMg_{12}$. Wu et al. [22] found that the grain size of melt-spun ribbon of Mg–10Ni–2Mm alloy was remarkably reduced by the increasing solidification rate. The microcrystalline, nanocrystalline, and amorphous microstructures were obtained by applying the surface velocities of the wheel of 3.1, 10.5, and 20.9 $m \cdot s^{-1}$, respectively. By applying the surface velocity of the wheel of 3.1 $m \cdot s^{-1}$, the melt-spun specimen obtained full crystalline with a considerable amount of coarse microcrystalline Mg and Mg_2Ni except for some Mm-rich particles. The amount of nanocrystalline phases significantly increased with the surface velocity of the wheel increasing to 10.5 $m \cdot s^{-1}$, and the microstructure was composed of a large amount of nanocrystalline phases of Mg and Mg_2Ni particles. A mixed microstructure containing amorphous and nanocrystalline phases was obtained at a surface velocity of the wheel of 20.9 $m \cdot s^{-1}$.

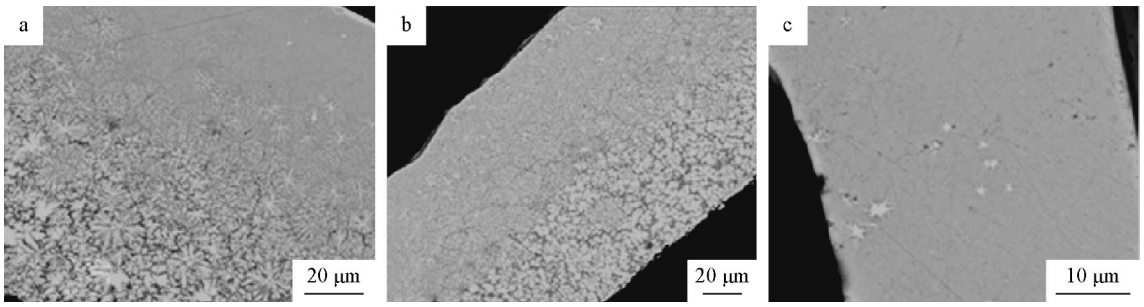

Fig. 3 Backscattered SEM images of RS $LaMg_{12}$ samples at different rotations speeds: **a** 3.1 $m{\cdot}s^{-1}$, **b** 10.5 $m{\cdot}s^{-1}$, and **c** 20.9 $m{\cdot}s^{-1}$

The optimal microstructure with a considerable amount of nanocrystalline Mg and Mg_2Ni in an amorphous matrix was expected to have the maximum hydrogen absorption capacity and excellent hydrogenation kinetics.

Zhang et al. [23] reported that the amorphous $Mg_{11}Y_2Ni_2$ alloy prepared by melt-spinning technique transformed into the crystalline $Mg_{11}Y_2Ni_2$ in metastable state at 279 °C and subsequently decomposed into Mg, $YMgNi_4$, and Y(Mg) solid solution in stable state at 366 °C. All the amorphous, metastable, and stable $Mg_{11}Y_2Ni_2$ alloys can be hydrogenated into MgH_2, Mg_2NiH_4, and YH_2/YH_3. However, the stable $Mg_{11}Y_2Ni_2$ alloy had slightly slower hydrogen absorption/desorption kinetics due to the worse dispersivity of YH_2/YH_3 and Mg_2NiH_4 [24].

Lin et al. [25] pointed out that the melt-spun $Mg_3LaNi_{0.1}$ alloy could absorb 2.7 wt% hydrogen at room temperature within 3 min and release completely at 241 °C. The melt-spun $Mg_3LaNi_{0.1}$ alloy decomposed to LaH_3, MgH_2, and Mg_2NiH_4 after the first hydrogenation, and a multiphase composite structure consisting of nanocrystalline LaH_2, Mg, and Mg_2Ni was obtained after dehydrogenation. Mg_2NiH_4 released hydrogen at 216 °C, which could benefit the dehydrogenation of MgH_2. Moreover, LaH_2 nanocrystals surrounding the MgH_2 crystallites would enhance the hydrogenation and dehydrogenation of MgH_2 by providing abundant hydrogen diffusion pathways along the phase boundaries and the intra-grains [26].

Kalincichenka et al. [27] found that the activation of the as-spun $Mg_{90}Ni_8RE_2$ alloy was successfully carried out at temperature of 385 °C and H_2 pressure of 3 MPa. Figure 4 presents the hydrogenation behavior of melt-spun and activated $Mg_{90}Ni_8RE_2$ under 2 MPa H_2 at temperatures between 50 and 300 °C [27]. It could be seen from Fig. 4 that activated $Mg_{90}Ni_8RE_2$ can reach reversible gravimetric hydrogen storage capacities of up to 5.5 wt% within 20 min, which was superior to the comparable melt-spun Mg-based alloys. The hydrogenation rates were rather high (up to 1.6 $wt\%{\cdot}min^{-1}$ at 300 °C). The dehydrogenation rates of the hydrogenated alloy depended strongly on temperature and pressure. The dehydrogenation at 0.1 MPa hydrogen back pressure was observed only above 250 °C because of thermodynamic reasons. The hydrogen uptake within 60 min increased with the number of cycles (up to 23 cycles), while the initial hydrogenation and dehydrogenation rates remained unchanged. This fact was most probably caused by the increase of the specific surface area of the ribbon. The microstructure of the $Mg_{90}Ni_8RE_2$ alloy remained nanocrystalline even after 23.5 h hydrogen absorption and desorption in one day.

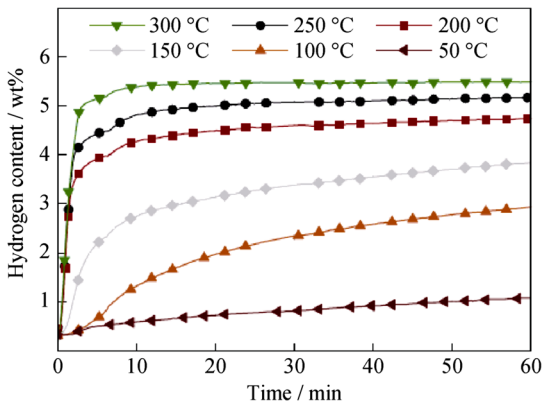

Fig. 4 Hydrogenation behavior of melt-spun and activated $Mg_{90}Ni_8RE_2$ under 2 MPa H_2 at temperatures between 50 and 300 °C

Lass [28] investigated that amorphous-crystalline composite ribbons of quaternary Mg-Ni-(Y, La)-Pd alloys were produced via rapidly solidification and used precursors for creating nanocrystalline hydrogen storage materials. The resulting materials demonstrated relatively high hydrogen capacity of around 4.5 wt% and excellent absorption/desorption kinetics at 573 K. Additionally, the alloys demonstrated reversible hydrogen storage at 473 K. $Mg_{85}Ni_{10}Y_{2.5}Pd_{2.5}$ fully absorbed and desorbed 4.6 wt% H in 90 min. The cyclability of the quaternary alloys demonstrated good stability with little loss in the maximum capacity through 8–10 cycles. This was attributed to the improved stability of the nanocrystalline structure attained via the Y and La additions. Thermodynamically, the enthalpy of the hydrogen absorption reaction was reduced

Table 2 Enthalpies and entropies of reaction for each alloy

Alloys	ΔH_r^{ABS}/(kJ·mol^{-1})	ΔS_r^{ABS}/(J·mol^{-1}·K^{-1})	ΔH_r^{DES}/(kJ·mol^{-1})	ΔS_r^{DES}/(J·mol^{-1}·K^{-1})
$Mg_{85}Ni_{10}Y_1Pd_4$	−67.7 ± 9.8	121.4 ± 15.6	−77.2 ± 9.8	134.0 ± 10.5
$Mg_{85}Ni_{10}La_1Pd_4$	−72.4 ± 5.9	130.6 ± 5.1	−77.6 ± 5.9	135.5 ± 10.4
$Mg_{85}Ni_{10}Y_{2.5}Pd_{2.5}$	−65.7 ± 9.9	117.3 ± 20.0	−77.4 ± 9.9	135.5 ± 7.6
$Mg_{85}Ni_{10}La_{2.5}Pd_{2.5}$	−69.4 ± 8.1	124.4 ± 6.6	−81.3 ± 8.1	140.8 ± 21.7

by 5 kJ·mol^{-1} in the quaternary alloys compared with Mg–MgH_2, while the entropy of reaction was also reduced (Table 2, [28]).

Wu et al. [29] found that the amorphous $Mg_{65}Ni_{27}La_8$ alloy prepared by melt spinning had a maximum discharge capacity of 558 mAh·g^{-1}. Some Mg_2NiH_4 nanocrystallites appeared in the alloy after charging. Most of them were less than 4 nm in diameter and metastable. These small nanocrystallites can readily be dehydrogenated and decomposed by discharging. Hydrogen atoms were stored in the amorphous phase and the Mg_2NiH_4 phases. The amorphous phase can absorb and desorb H atoms effectively and efficiently, and facilitate the dehydrogenation of these small Mg_2NiH_4 nanocrystallites. The high discharge capacity was attributed to a synergistic effect of the small nanocrystallites of Mg_2Ni hydrides and the amorphous phase around them. Hydrogen atoms were stored in two regions in the amorphous $Mg_{65}Ni_{27}La_8$ alloy after charging, i.e., one part in the amorphous phase and the other one in the Mg_2NiH_4 phases. The charge/discharge process consisted of four steps. These four steps were corresponding to the hydrogen absorption in the amorphous phase, the formation of the Mg_2NiH_4 phases, the dehydrogenation of the Mg_2NiH_4 phases, and the hydrogen desorption from the amorphous phase, respectively. The amorphous phase in the alloy played an important role in achieving the high discharge performance and cycle durability of the electrode. The Mg_2NiH_4 nanocrystallites with size of less than 4 nm can be easily dehydrogenated by discharging, which was catalyzed by the amorphous phase around them. The high discharge capacity can be attributed to the synergistic effect of the small Mg_2Ni hydrides and the amorphous phase in the alloy. The Mg_2NiH_4 nanocrystallines with size of more than 4 nm remained in the discharged alloy were likely to grow up during further charge/discharge cycles, which was one of the reasons to cause the decay of the discharge capacity.

Li et al. [30] investigated the dehydrogenation of the amorphous $(Mg_{60}Ni_{25})_{92}La_8$ alloy by both galvanostatic and non-isothermal methods and obtained a maximum discharge capacity of 558 mAh·g^{-1} at room temperature and 4.5 wt% of released hydrogen at a heating rate of 5 °C·min^{-1}. The non-isothermal dehydrogenation process was divided into two steps. In the first step, the alloy released 2 wt% H, which corresponded to the amorphous phase dehydrogenation and the growth of Mg_2NiH_4. In the second step, the alloy released 2.5 wt% H, corresponding to the dehydrogenation of Mg_2NiH_4 accompanied by the formation of LaH_2. During the charging process, the amorphous phase partially crystallized into a Mg_2NiH_4 phase. It was found that the hydrogen storage capacity of the amorphous phase was larger than that of Mg_2NiH_4. The solute H atoms dissolved in the amorphous phase could be easily released at room temperature, which suggested that restraining the amorphous phase crystallization during charging could be useful to improve the discharge capacity.

Shao et al. [31] investigated the phase and morphology evolution study of ball-milled Mg–Co hydrogen storage alloys. At the beginning of the milling, Co was dispersed on the surface of Mg particle. Then, Mg particles were cracked into small ones. After 25 h, FCC Co phase formed and Co particles dissolved into Mg particles. From 25 to 50 h, the particle size was greatly reduced with the milling time. BCC phase appeared after 45 h milling. After 100 h, only BCC phase was observed. Differential scanning calorimetry (DSC) curves of $Mg_{50}Co_{50}$ alloys milled for 50 and 100 h showed two obvious exothermic peaks. These two peaks shifted to higher temperatures with the milling time due to the less presence of remaining catalytic Co phase. For the samples milled for 300 h, a broad exothermic peak consisting of two overlapped peaks was observed, which may result from round-shape particles with few defects and surface area on the particle surface. The $Mg_{50}Co_{50}$ alloy milled for 100 h absorbed more hydrogen at 258 than at 323 K. The absorption process by PCT measurements under these conditions was thermodynamically dominant. The $Mg_{50}Co_{50}$ alloy milled for 50 h showed better kinetics and absorption capacity than that milled for 100 h, because of the catalytic effect of residual Co in the 50 h sample. The 300 h sample probably had more inner defects from longer milling process.

Ball milling of $Mg_{75}Ni_{25}$ powders resulted in a Mg + Ni → Mg_2Ni solid-state reaction, while some portion of FCC-Ni did not take part in the reaction. During the hydrogenation of Mg_2Ni powder milled for 10 h, the $Mg_2NiH_{0.3}$ hexagonal solid solution and the monoclinic Mg_2NiH_4 hydride phase nucleated. There are partial desorbed states in the sample, indicating that the solid solution

was more stable during the dehydrogenation process, having practically the same average crystallite size ($D = 33$ nm) and similar size distribution. Despite the decreasing hydrogen content during desorption at 300 °C; moreover, the monoclinic Mg_2NiH_4 crystals grew up to 50 nm, while its distribution became significantly broader. It was also confirmed that the dehydrogenation of both hydrides occurred in a single-step process. The desorption-induced changes in the relative amount of the hydride phases indicated that the gradual volumetric decreases of Mg_2NiH_4 and $Mg_2NiH_{0.3}$ were not simultaneous. At the beginning of the dehydrogenation process, the decomposition of the solid solution was more intensive, while later on the conversion of Mg_2NiH_4 became dominant [32].

Liu et al. [33] proved that hydrogen plasma–metal reaction (HPMR) was effective to prepare nanoparticles of Mg and other transition metals in large scale because of plasma promotion. The nanoparticle formation process can be divided into five steps: the formation of active hydrogen ion or atom, the hydrogen over-saturation dissolving, the hydrogen bubble formation, the evaporation of metal vapor together with hydrogen bubble, and the condensation of metal vapor. Metallic nanoparticles were fabricated by HPMR method when the starting metal was a non-hydride formation element, whereas metal hydride nanoparticles were produced when the starting metal was a hydride formation element except for Mg. The pure and nanostructured Mg_2Ni, Mg_2Co, Mg_2Cu, and Mg_2FeH_6 were successfully prepared by gas–solid reaction of hydrogen and mixture of Mg and corresponding transition metal nanoparticles. The reaction temperature was much lower than the hydrogen combustion approach; therefore, the nanostructure can be kept through the reaction. The hydrogen absorption and desorption rates were promoted, and the sorption temperatures decreased. The kinetic properties were improved greatly because of the short diffusion distance and large specific surface area. The thermodynamic properties of the nanostructured Mg_2Ni were improved only slightly.

These researchers also prepared Mg-6.9 at% Zn ultrafine particles by HPMR method [34]. The electron microscopy study revealed that they were spherical in shape with particle size in the range of 100–700 nm. Each fine particle was composed of single crystal structure of α-Mg(Zn) solid solution and amorphous structure of Mg-Zn alloy. After one absorption and desorption cycle, these ultrafine particles (UFPs) transformed from the single crystal into the nanocrystalline structure and the mean particle size changed from 400 to 250 nm (Fig. 5, [34]). It was found that the Mg-Zn ultrafine particles could absorb 5.0 wt% hydrogen in 20 min at 573 K and accomplished a high hydrogen storage capacity of 6.1 wt% at 573 K. The fine particle size, nanocrystalline structure, and the low oxide content of the obtained sample promoted the hydrogen sorption process with low hydrogen absorption activation energy of 56.3 kJ·mol^{-1}. The hydrogen reversible capacities were as large as 4.6 wt%, 4.9 wt%, 5.1 wt%, and 5.2 wt% at 573, 598, 623, and 648 K, respectively. The Mg-Zn UFPs could absorb 6.1 wt% H at 573 K, even though the addition of Zn deteriorated the hydrogen absorption capacity. The obtained value of the hydride formation enthalpy for the Mg–Zn UFPs was −74.0 kJ·mol^{-1}. These researchers also prepared the Mg–10.2 at% V composite nanoparticles by HPMR method. The Mg nanoparticles were hexagonal in shape with average particle size of 100 nm. The spherical VH_2 nanoparticles with mean diameter of 10 nm dispersed evenly on the surface of the Mg nanoparticles. After the hydrogen absorption, the size of MgH_2 nanoparticles decreased to 60 nm, while the size of V nanoparticles was still about 10 nm. The Mg–V composite nanoparticles can absorb 3.8 wt% hydrogen in less than 30 min even at 473 K, and accomplish a high hydrogen storage capacity of 5.0 wt% in less than 5 min at 623 K. They released 4.0 wt% hydrogen in less than 15 min at 573 K. The catalytic effect of V nanoparticles, the nanostructure and the low oxide content of the Mg particles resulted in the low hydrogen absorption and desorption activation energies of 71.2 and 119.4 kJ·mol^{-1}, respectively. The enhanced hydrogen sorption rate and storage capacity were due to the improved kinetics rather than the change in enthalpy [35].

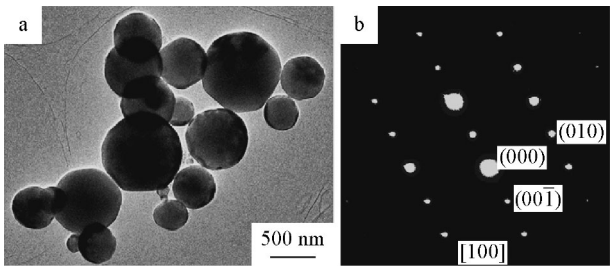

Fig. 5 TEM bright-field image of the as-prepared Mg–Zn ultra particles **a** and electron diffraction pattern of one particle **b**

Magnesium nanoparticles confined in carbon aerogels were successfully synthesized through hydrogenation of infiltrated dibutyl magnesium followed by hydrogen desorption at 623 K. The average crystallite size of Mg nanoparticle was calculated to be 19.3 nm based on XRD analyses. The size of MgH_2 particle mainly was distributed in the range from 5.0 to 20.0 nm with a majority portion of smaller than 10.0 nm. The hydrogenation and dehydrogenation enthalpies of the confined Mg were determined to be (−65.1 ± 1.56) kJ·mol^{-1} and (68.8 ± 1.03) kJ·mol^{-1} by pressure–composition–temperature tests, respectively, slightly lower than the corresponding enthalpies for pure

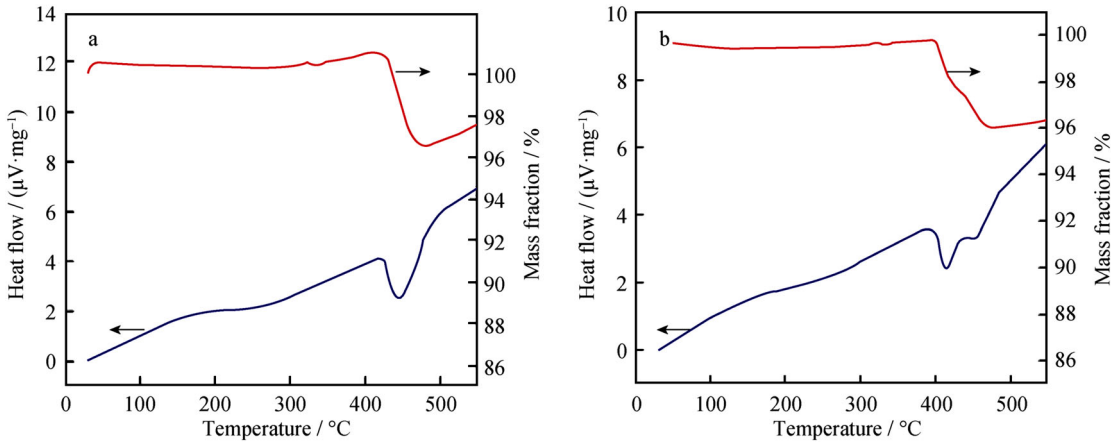

Fig. 6 Thermal gravimetric/differential thermal analyzer (TG/DTA) curves of ultrafine hydrogenated pure Mg **a** and Mg–Ti **b** particles

Mg. In addition, the apparent activation energy for hydrogen absorption was determined to be 29.4 $kJ \cdot mol^{-1}$, much lower than that of the micro-size Mg particles. These results indicated that the thermodynamic and absorption kinetic properties of confined Mg nanoparticles can be significantly improved due to the nano-sized effect [36].

Stéphane et al. [37] used arc plasma method to produce ultrafine pure Mg and Mg–Ti particles for hydrogen storage. Most of the ultrafine Mg and Mg–Ti particles have a hexagonal shape. Their particle size was in the range of 50–700 nm. The hydrogenation enthalpy of Mg–Ti powders was determined to be about -67 $kJ \cdot mol^{-1}$, while -78.6 $kJ \cdot mol^{-1}$ measured for pure Mg powders. After hydrogenation, some of the large Mg particles cannot be fully hydrogenated. This explained the fact that the maximum hydrogen storage capacity of the Mg powders was lower than the theoretical capacity of Mg. The onset dehydriding temperature of hydrogenated Mg–Ti powders was measured to be 386 °C, which was significantly lower than the dehydriding temperature (423 °C) of hydrogenated pure Mg powders (Fig. 6, [37]). Therefore, the addition of Ti into Mg through arc evaporation method can effectively improve the thermodynamic properties of Mg for hydrogen storage.

4 Using catalysts for hydrogenation/dehydrogenation process

The use of catalysts is an important pathway to improve surface kinetics. Several catalysts were applied such as transition metal, metal oxides, carbon, and halides. The catalytic effect may consist of various mechanisms, such as enhancing the rate of hydrogen dissociation, accelerating the diffusion of hydrogen, or modifying the surface of magnesium.

Song et al. [38] employed La_2O_3–CaO composite additive to accelerate the hydrogen absorption/desorption rate of the Mg_2Ni alloy. The composite additive was ball milled with Mg_2Ni hydride to produce Mg_2Ni–5 wt% La_2O_3–5 wt% CaO composite. The composite additive significantly reduced the thermal stability of Mg_2NiH_4. The onset decomposition temperature of the hydrogenated composite was 470 K, 21 K lower than that of the pure Mg_2NiH_4. Meanwhile, the composite presented accelerated hydriding/dehydriding kinetic properties. It absorbed 1.61 wt% H at 373 K in 2 h and released 2.44 wt% H at 573 K in 1,200 s, while the absorbed and desorbed hydrogen of the pure Mg_2NiH_4 were only 0.78 wt% and 1.32 wt%, respectively. The improvement in the hydrogen storage properties of the Mg_2Ni alloy by the adoption of La_2O_3–CaO additive was ascribed to the modified catalytic effects of La_2O_3 and CaO in the composite.

Kubota et al. [39] investigated the catalytic effects of non-milled graphite, milled graphite at hydrogen atmosphere, and milled graphite at argon atmosphere. Three types of the Mg–C materials were synthesized by ball milling method from the carbon materials with different crystallinities. All the Mg–C materials were multiphase state composed of Mg and the Mg–C compounds with nanocrystalline or amorphous structure. The Mg–C compounds possessed the similar chemical bonding state as Mg_2C_3. The amount of the Mg–C phase increased when the crystallinity of carbon materials was lower. For the hydrogen absorption reaction, the kinetics of the Mg–C compounds was slower than that of Mg, and the hydrogenation of Mg and the compounds occurred at around 150 and 350 °C, respectively. By the hydrogenation, the MgH_2 phase formed in all the materials. In addition, it was indicated that the C–H bonds were generated in Mg-milled graphite at argon atmosphere during the hydrogen absorption of the Mg–C compounds. The hydrogen

desorption reactions were classified into two processes. The first hydrogen desorption at 350 °C was caused by the separated thermal decomposition of MgH_2. In the second process, the hydrogen was desorbed at around 400 °C by the interaction between Mg and the C–H bonds to form the Mg–C phase. The Mg–C materials exhibited different hydrogen storage properties with the crystallinity of carbon materials as the starting material. The high-crystalline graphite was difficult to form the carbide phase because graphite structure was quite stable and Mg was unable to be intercalated into the layers of graphite, resulting in that Mg separately absorbed and desorbed hydrogen. In the case of the low-crystalline graphite, about 3.7 wt% hydrogen can be absorbed and desorbed below 420 °C via the formation and decomposition of the Mg–C phase.

Yuan and Lototskyy et al. [40, 41] used hydriding combustion synthesis (HCS) and mechanical milling (MM) to prepare the composites Mg95-Pd*m*/MWCNTs5−*m* ($m = 0, 1, 2, 3, 4, 5$). The Pd/MWCNTs catalyst can significantly increase the hydrogenation degree of Mg during the HCS process, and both the hydriding and dehydriding properties of the Pd/MWCNTs added composites were improved. There was a synergistic effect of MWCNTs and Pd on the hydrogen storage properties of the composites. For hydriding, the Mg95-Pd3/MWCNTs2 composite required only 100 s to reach its saturated hydrogen capacity of 6.67 wt% at 473 K. For dehydriding, Mg95-Pd3/MWCNTs2 possessed the best properties, desorbing 6.66 wt% hydrogen within 1,200 s at 573 K. The dehydrogenation activation energy of the Mg95-Pd3/MWCNTs2 was 78.6 $kJ \cdot mol^{-1}$. The addition of Pd/MWCNTs was favorable to the improvement of hydrogen storage properties of Mg-based materials prepared by HCS + MM.

Magnesium hydride was ball-milled with 7 wt% various metal halide additives (ZrF4, TaF5, NbF5 and TiCl3) by Malka et al. [42]. The metal halides except ZrF_4 took part in the partial and full disproportionation reactions directly after milling in the first desorption/absorption cycle. The catalytic effect of metal halides on the Mg hydrogenation/dehydrogenation process was caused by the formation of pure transition metal and/or the MgF_2 phase, which led to the influence of two simultaneous factors on the sorption properties of the MgH_2. This effect may be caused by the presence of the F anion, which weakened the Mg–H bonding, led to the formation of MgF_2, and provided an electron-rich center to trap the transition metal atoms. In addition, the F anion may tailor the electronic structure of the transition metal atom to influence its activity for hydrogen dissociation/recombination. This was essential for the catalytic behavior of these additives. It was important to note the change in the valence state of the metal halides during processing. It was shown that NbF_5, TaF_5, and particularly $TiCl_3$ took part in the disproportionation reactions that created a significant amount of structural defects.

Mg–23.5 wt% Ni–5 wt% Cu alloy was prepared by gravity casting method in a large quantity (approximately 7.5 kg), and then melt spun and heat treated [43]. Thereafter, 30 wt% $LaNi_5$, 10 wt% nano-sized Nb_2O_5, and 30 wt%$LaNi_5$ + 10 wt% nano-sized Nb_2O_5, respectively, were added to the prepared Mg–23.5 wt% Ni–5 wt% Cu alloy by reactive mechanical grinding. The (Mg–23.5 Ni–5Cu)–10 Nb_2O_5 sample showed the highest hydrogen storage capacity and hydriding and dehydriding rates, followed by (M-23.5N-5Cu)-30$LaNi_5$ and (Mg–23.5Ni–5Cu) –30$LaNi_5$–10Nb_2O_5. The addition of Nb_2O_5 was believed to increase the hydrogen -storage capacity and hydriding and dehydriding rates due to the brittleness and small particle size, which led to the pulverization of Mg–23.5Ni–5Cu during reactive mechanical grinding. The activation of the (Mg–23.5Ni–5Cu)-10Nb_2O_5 sample was completed only after the second cycle. This sample absorbed 2.43 wt% in 10 min and 3.07 wt% in 60 min at 573 K under 1.2 MPa H_2, and desorbed 3.08 wt% in 20 min at 573 K under 0.1 MPa H_2 at $n = 2$ (Fig. 7, [43]).

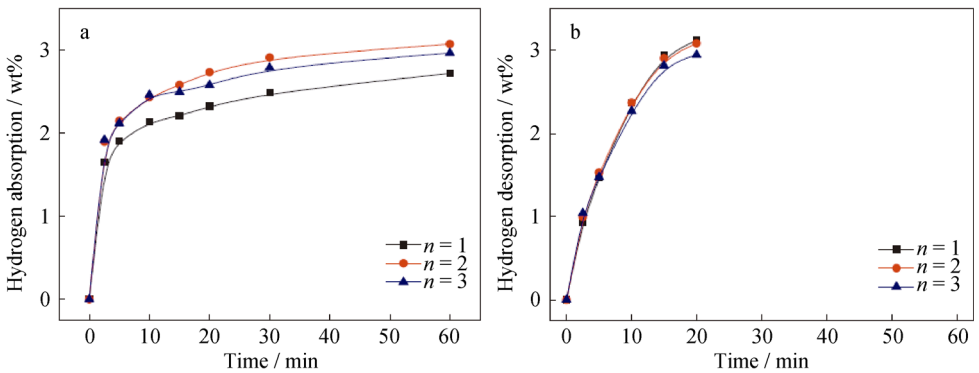

Fig. 7 Variation of hydrogen absorption and desorption with number of cycles (n) for (Mg–23.5Ni–5Cu)–10Nb_2O_5 at 573 K under 0.1 MPa H_2: **a** hydrogen absorption and **b** hydrogen desorption

Long et al. [44] prepared Mg-5 wt% Ce oxide nanocomposite through arc plasma method. CeO_2 transformed into Ce_2O_3 after arc evaporation, and nanoscale Ce_2O_3 particles were attached on the surface of Mg particles, forming a core–shell structured metal-oxide nanocomposite. The hydrogenation and dehydrogenation enthalpies of the composite were calculated to be −71.00 and 75.41 kJ·mol^{-1}, respectively, while the activation energy for hydrogen absorption was 47.75 kJ·mol^{-1}. In addition, the composite can absorb 4.07 wt% of hydrogen at 323 K in 10 h. These results revealed that the minor addition of Ce oxide in Mg through arc plasma method was able to significantly improve the hydrogen absorption kinetics of Mg.

Singh et al. [45] investigated the effect of different sized CeO_2 nanoparticles on decomposition and hydrogen absorption kinetics of magnesium hydride. A small amount of admixing of the above said catalysts with MgH_2 exhibited improved hydrogen storage properties. Among these different sizes of CeO_2 nanoparticles, 2 wt% admixed CeO_2 with a particle size of 10–15 nm led to the decrease of desorption temperature by 50 K. Moreover, it also showed 1.5 times absorption kinetics with respect to pure MgH_2. The hydrogenation/dehydrogenation properties were measured by gas reaction controller.

Han et al. found that MoS_2 had a superior catalytic effect over MoO_2 on improving the hydrogen kinetic properties of MgH_2 [46]. DTA results indicated that the desorption temperature decreased from 662.10 K of the pure MgH_2 to 650.07 K of the MgH_2 with MoO_2 and 640.34 K of that with MoS_2. Based on the Kissinger plot, the activation energy of the hydrogen desorption process was estimated to be (101.34 ± 4.32) kJ·mol^{-1} of the MgH_2 with MoO_2 and (87.19 ± 4.48) kJ·mol^{-1} of that with MoS_2, indicating that the dehydriding process energy barrier of MgH_2 can be reduced. The enhancement of the hydriding/dehydriding kinetics of MgH_2 was attributed to the presence of MgS and Mo or MgO and Mo which catalyzed the hydrogen absorption/desorption behavior of MgH_2. The detailed comparisons between MoS_2 and MoO_2 suggested that S anion had superior properties than O anion on catalyzing the hydriding/dehydriding kinetics of MgH_2.

5 Using thin film hydride

Owing to the advantages of thin film metal hydrides such as large surface area, fast charging, and discharging rate for hydrogen, protective surface coating could be done to stop poisoning by oxygen, and activation of thin film hydrides was possible by coating with a layer of catalytic.

Liu et al. [47] investigated the hydrogen storage properties of a series of Mg–La–Pd trilayer films (La = 0.5–9.0 nm). When the thickness of La layer was larger than 3 nm, the distribution of La element became homogeneous. The hydrogen storage properties of the films under 0.1 MPa H_2 and at 298 K were investigated by measuring their resistance and optical transmittance during the hydrogenation. The hydrogenation of the La-3.0 nm film saturated within 14 s and possessed the fastest absorption kinetics compared with other Mg–La–Pd films. The further increase of La thickness decreased the hydrogenation rate due to the decreased hydrogen diffusion rate through this layer. The La-3.0 nm film also exhibited the fast hydrogen desorption rate in air at room temperature. It released 80 % of hydrogen within 60 min. The electrochemical properties of the Mg–La–Pd films were carried out in 6 mol·L^{-1} KOH with a three-electrode cell. Among these films, the La-3.0 nm film possessed the largest anodic area and anodic peak current, as well as the highest maximum discharge capacity of 377.8 mAh·g^{-1}.

Wang et al. [48] used direct current magnetron cosputtering to prepare Mg–Y thin films capped with Pd. It was found that Mg alloyed with Y in film state formed ultrafine nanocrystalline intermetallic compounds. The structure together with the catalytic effect of Y gave rise to a high electrochemical hydrogen storage capacities and superior activation properties. It was worthy to noting that $Mg_{78}Y_{22}$ film achieved a high discharge capacity of 1,590 mAh·g^{-1} without requiring activation process. Moreover, Mg alloyed with Y effectively improved the cyclic stability of Mg-based films ascribed to the anti-corrosion role of Y. For

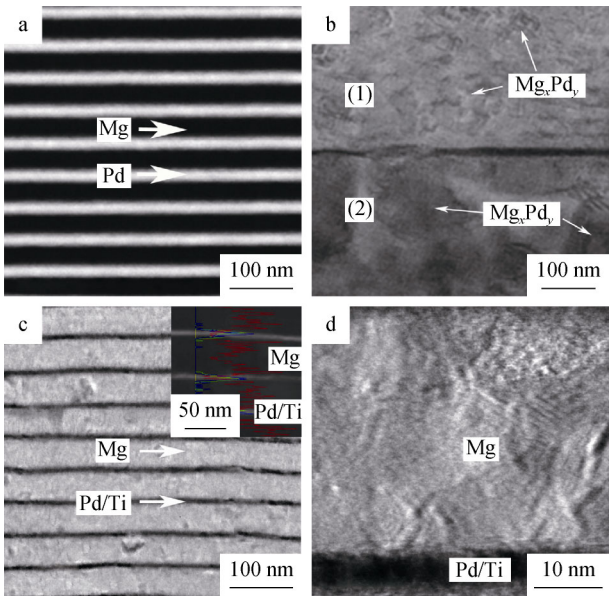

Fig. 8 Cross-sectional TEM images of **a** as-deposited Mg/Pd multilayer film, **b** Mg/Pd multilayer film after hydrogenation, **c** low-resolution (inset: EDS line scan profiles), and **d** high-resolution image of Ti/Mg/Ti/Pd multilayer film after hydrogenation at 200 °C

$Mg_{37}Y_{63}$ film, more than 92 % of the maximum discharge capacity can be maintained after 100 charge/discharge cycles.

Jung et al. [49] investigated the microstructural and hydrogen storage properties of 60 multilayer Mg/Pd and Ti/Mg/Ti/Pd films (Fig. 8, [49]) using an ultra-high-vacuum (UHV) DC magnetron sputtering system. The hydrogen absorption capacity of the Ti/Mg/Ti/Pd film was found to be 1.7 wt%, 3.5 wt%, and 4.7 wt% at 50, 100, and 150 °C, respectively, while that of the Mg/Pd film was measured at significantly lower values, 0.18 wt%, 0.65 wt%, and 1.35 wt%. The hydrogen absorption capacity for the Mg/Pd and Ti/Mg/Ti/Pd films was greatly dependent upon the formation of Mg–Pd intermetallic phases during the hydrogenation process. Our results demonstrated that Ti interlayers in the Ti/Mg/Ti/Pd film played a crucial role in preventing the formation of Mg–Pd intermetallic phases, which originated from the inter-diffusion of Mg and Pd atoms during hydrogenation, and thus resulting in an improved hydrogen storage capacity.

6 Conclusion and future prospects

All these approaches resulted in promising results, such as improved development on hydrogenation, thermodynamic, and kinetics of metal hydrides; however, the states of Mg and Mg-based alloys are still far from meeting the aimed target for fuel cell which is used to transport application. Therefore, further research work is needed to carry on as follows: (1) the hydrogen absorption and desorption velocity of Mg and Mg-based alloys should be further enhanced, and the temperature of hydrogenation and dehydrogenation reaction even at normal pressure and temperature should be lowered; (2) the high sensitivity and anti-oxidation in hydrogen gas atmosphere containing impurity gas, such as O_2, N_2, and air, should be strengthened; (3) although ultra-particle, micro- and nanocrystalline, or amorphous structure can improve the thermodynamic and kinetics of hydrogen absorption and desorption of Mg and Mg-based alloys, the real status such as hydrogenation and dehydrogenation temperature and velocity could not satisfy; therefore, the advantage and disadvantage of nanometer effect and amorphous should be further investigated; and (4) catalyst-enhanced Mg and Mg-based alloy hydrides improve activation energies and the kinetics of surface interactions; the addition of the catalysts (REs, etc.) and the using of preparation technique (ball milling, etc.) modify hydrogen absorption and desorption properties of Mg and Mg-based alloy owing to the defects and decreasing particle sizes. More work is needed to evaluate the catalytic mechanism and find more effective catalysts on other kinetics such as nucleation and diffusion.

Acknowledgments This work was financially supported by the National Natural Science Foundation of China (Nos. 51161015 and 51371094).

References

[1] Broom DP. Hydrogen Storage Materials: The Characterization of Their Storage Properties. London: Springer; 2011. 1.
[2] Jain IP, Lal C, Jain A. Hydrogen storage in Mg: almost promising material. Int J Hydrogen Energy. 2010;35(10):5133.
[3] Wang DH, Xia JH, Zhang S. Microstructure of nano precursors of La–Mg hydrogen storage alloy synthesized by sol–gel technology at different pH values. Rare Met. 2012;31(5):466.
[4] Zhang YH, Li BW, Ren HP, Ding XX, Liu XG, Chen LL. An investigation on hydrogen storage kinetics of nanocrystalline and amorphous $Mg_2Ni_{1-x}Co_x$ ($x = 0$–0.4) alloy prepared by melt spinning. J Alloys Compd. 2011;509(6):2808.
[5] Hong SH, Kwon SN, Kwak YJ, Song MY. Hydrogen-storage characteristics of Cu, Nb_2O_5, and NbF_5-added Mg–Ni alloys. Mater Res Bull. 2012;47(2):172.
[6] Kalincichenka S, Röntzsch L, Baehtz C, Kieback B. Hydrogen desorption kinetics of melt-spun and hydrogenated $Mg_{90}Ni_{10}$ and $Mg_{80}Ni_{10}Y_{10}$ using in situ synchrotron, X-ray diffraction and thermogravimetry. J Alloys Compd. 2010;496(1–2):608.
[7] Hu L, Han SM, Li JH, Yang C, Li Y, Wang MZ. Phase structure and hydrogen absorption property of $LaMg_2Cu$. Mater Sci Eng, B. 2010;166(3):209.
[8] Ren HP, Zhang YH, Li BW, Zhao DL, Guo SH, Wang XL. Influence of the substitution of La for Mg on the microstructure and hydrogen storage characteristics of $Mg_{20-x}La_xNi_{10}$($x = 0$–6) alloys. Int J Hydrogen Energy. 2009;34(3):1429.
[9] Liu BZ, Li JH, Han SM, Hu L, Pei LC, Wang MZ. Microstructures and hydrogen storage properties of $LaMg_{8.40}Ni_{2.34-x}Al_x$ alloys. J Alloys Compd. 2012;526(15):6.
[10] Pei LC, Han SM, Wang JS, Hu L, Zhao X, Liu BZ. Hydrogen storage properties and phase structures of RMg_2Ni (R = La, Ce, Pr, Nd) alloys. Mater Sci Eng B. 2012;177(18):1589.
[11] Pei LC, Han SM, Hu L, Zhao X, Liu YQ. Phase structure and hydrogen storage properties of $LaMg_{0.93}Ni_{0.21}$ alloy. J Rare Earth. 2012;30(6):534.
[12] Xie DH, Li P, Zeng CX, Sun JW, Qu XH. Effect of substitution of Nd for Mg on the hydrogen storage properties of Mg_2Ni alloy. J Alloys Compd. 2009;478(1–2):96.
[13] Kalisvaart WP, Harrower CT, Haagsma J, Zahiri B, Luber EJ, Ophus C, Poirier E, Fritzsche H, Mitlin D. Hydrogen storage in binary and ternary Mg-based alloys: a comprehensive experimental study. Int J Hydrogen Energy. 2010;35(5):2091.
[14] Knotek V, VoJtěch D. Electrochemical hydriding performance of Mg−TM−Mm (TM = transition metals, Mm = mischmetal) alloys for hydrogen storage. Trans Nonferrous Met Soc China. 2013;23(7):2047.
[15] Nielsen TK, Besenbacher F, Jensen TR. Nanoconfined hydrides for energy storage. Nanoscale. 2011;3(5):2086.
[16] Nielsen TK, Manickam K, Hirscher M, Besenbacher F, Jensen TR. Confinement of MgH_2 nanoclusters within nanoporous aerogel scaffold materials. ACS Nano. 2009;3(11):3521.
[17] Yao X, Zhu ZH, Cheng HM, Lu GQ. Hydrogen diffusion and effect of grain size on hydrogenation kinetics in magnesium hydrides. J Mater Res. 2011;23(2):336.
[18] Zaluska A, Zaluski L, Ström-Olsen JO. Nanocrystalline magnesium for hydrogen storage. J Alloy Compd. 1999;288(1–2):217.
[19] Cheung S, Deng WQ, van Duin ACT, Goddard WA. MgH reactive force field for magnesium hydride systems. J Phys Chem A. 2005;109(5):851.

[20] Wagemans RW, van Lenthe JH, de Jongh PE, van Dillen AJ, de Jong KP. Hydrogen storage in magnesium clusters: quantum chemical study. J Am Chem Soc. 2005;127(47):16675.
[21] Poletaev AA, Denys RV, Solberg JK, Tarasov BP, Yartys VA. Microstructural optimization of $LaMg_{12}$ alloy for hydrogen storage. J Alloys Compd. 2011;509(S2):S633.
[22] Wu Y, Xing N, Lu ZC, Han W, Zhou SX, Solberg JK, Yartys VA. Microstructural evolution of melt-spun Mg–10Ni–2Mm hydrogen storage alloy. Trans Nonferrous Met Soc China. 2011;21(1):121.
[23] Zhang QA, Zhang LX, Wang QQ. Crystallization behavior and hydrogen storage kinetics of amorphous $Mg_{11}Y_2Ni_2$ alloy. J Alloys Compd. 2013;551:376.
[24] Chen HX, Wang ZM, Zhou HY, Ni CY, Deng JQ, Yao QR. Hydrogen storage properties and thermal stability of amorphous $Mg_{70}(RE_{25}Ni_{75})_{30}$ alloys. J Alloys Compd. 2013;563:1.
[25] Lin HJ, Ouyang LZ, Wang H, Liu JW, Zhu M. Phase transition and hydrogen storage properties of melt-spun $Mg_3LaNi_{0.1}$ alloy. Int J Hydrogen Energy. 2012;37(1):1145.
[26] Révész Á, Kis-Tóth Á, Varga LK, Schafler E, Bakonyi I, Spassov T. Hydrogen storage of melt-spun amorphous $Mg_{65}Ni_{20}Cu_5Y_{10}$ alloy deformed by high-pressure torsion. Int J Hydrogen Energy. 2012;37(7):5769.
[27] Kalincichenka S, Röntzsch L, Riedl T, Weißgärber T, Kieback B. Hydrogen storage properties and microstructure of melt-spun $Mg_{90}Ni_8RE_2$ (RE = Y, Nd, Gd). Int J Hydrogen Energy. 2011;36(17):10808.
[28] Lass EA. Hydrogen storage in rapidly solidified and crystallized Mg–Ni–(Y, La)–Pd alloys. Int J Hydrogen Energy. 2012;37(12):9716.
[29] Wu DC, Liang GY, Li L, Wu HB. Microstructural investigation of electrochemical hydrogen storage in amorphous Mg–Ni–La alloy. Mater Sci Eng B. 2010;175(3):248.
[30] Li L, Wu DC, Liang GY, Sun ZB, Guo YL. The dehydrogenation process of amorphous $(Mg_{60}Ni_{25})_{92}La_8$ alloy. J Alloys Compd. 2009;474(1–2):378.
[31] Shao HY, Matsuda J, Li HW, Akiba E, Jain A, Ichikawa T, Kojima Y. Phase and morphology evolution study of ball milled Mg–Co hydrogen storage alloys. Int J Hydrogen Energy. 2013;38(17):7070.
[32] Révész Á, Marcell G, Spassov T. Microstructural evolution of ball-milled Mg–Ni powder during hydrogen sorption. Int J Hydrogen Energy. 2013;38(20):8342.
[33] Liu T, Shen HL, Liu Y, Xie L, Qu JL, Shao HY, Li XG. Scaled-up synthesis of nanostructured Mg-based compounds and their hydrogen storage properties. J Power Sources. 2013;227:86.
[34] Liu T, Zhang TW, Qin CG, Zhu M, Li XG. Improved hydrogen storage properties of Mg–V nanoparticles prepared by hydrogen plasma-metal reaction. J Power Sources. 2011;196(22):9599.
[35] Liu T, Zhang TW, Zhang XZ, Li XG. Synthesis and hydrogen storage properties of ultrafine Mg–Zn particles. Int J Hydrogen Energy. 2011;36(5):3515.
[36] Liu YN, Zou JX, Zeng XQ, Wu XM, Tian HY, Ding WJ, Wang J, Walter A. Study on hydrogen storage properties of Mg nanoparticles confined in carbon aerogels. Int J Hydrogen Energy. 2013;38(13):5302.
[37] Stéphane P, Zou JX, Zeng XQ, Sun HQ, Ding WJ. Preparation and hydrogen storage properties of ultrafine pure Mg and Mg–Ti particles. Trans Nonferrous Met Soc China. 2012;22(8):1849.
[38] Song JZ, Han SM, Fu RD. Effect of La_2O_3–CaO composite additive on the hydrogen storage properties of Mg_2Ni alloy. Mater Sci Eng B. 2014;188(1–3):114.
[39] Kubota A, Miyaoka H, Tsubota M, Shimoda K, Ichikawa T, Kojima Y. Synthesis and characterization of magnesium-carbon compounds for hydrogen storage. Carbon. 2013;56:50.
[40] Yuan JG, Zhu YF, Li Y, Zhang L, Li LQ. Effect of multi-wall carbon nanotubes supported palladium addition on hydrogen storage properties of magnesium hydride. Int J Hydrogen Energy. 2014;39(19):10184.
[41] Lototskyy M, Sibanyoni JM, Denys RV, Williams M, Pollet BG, Yartys VA. Magnesium–carbon hydrogen storage hybrid materials produced by reactive ball milling in hydrogen. Carbon. 2013;57:146.
[42] Malka IE, Pisarek M, Czujko T, Bystrzycki J. A study of the ZrF_4, NbF_5, TaF_5, and $TiCl_3$ influences on the MgH_2 sorption properties. Int J Hydrogen Energy. 2011;36(20):12909.
[43] Hong SH, Kwon SN, Bae JS, Song MY. Hydrogen storage characteristics of melt spun Mg–23.5Ni–5Cu alloys mixed with $LaNi_5$ and/or Nb_2O_5. J Ind Eng Chem. 2012;18(1):61.
[44] Long S, Zou JX, Liu YN, Zeng XQ, Ding WJ. Hydrogen storage properties of a Mg–Ce oxide nano-composite prepared through arc plasma method. J Alloys Compd. 2013;580(S1):167.
[45] Singh RK, Sadhasivam T, Sheeja GI, Singh P, Srivastava ON. Effect of different sized CeO_2 nano particles on decomposition and hydrogen absorption kinetics of magnesium hydride. Int J Hydrogen Energy. 2013;38(14):6221.
[46] Jia YH, Han SM, Zhang W, Zhao X, Sun PF, Liu YQ, Shi H, Wang JS. Hydrogen absorption and desorption kinetics of MgH_2 catalyzed by MoS_2 and MoO_2. Int J Hydrogen Energy. 2013;38(5):2352.
[47] Liu T, Cao YR, Li H, Chou WS, Li XG. Superior hydrogen storage and electrochemical properties of Mg–La–Pd tri-layer films at room temperature. J Power Sour. 2014;267:598.
[48] Wang YY, Xin GB, Li W, Wang W, Wang CY, Zheng J, Li XG. Superior electrochemical hydrogen storage properties of binary Mg–Y thin films. Int J Hydrogen Energy. 2014;39(9):4373.
[49] Jung H, Yuh J, Cho S, Lee W. Effects of Ti interlayers on microstructures and hydrogen storage capacity in Mg/Pd multilayer thin films. J Alloys Compds. 2014;601:63.

Dong-Liang Zhao graduated from Central Iron and Steel Research Institute in 1993. Since then he has been working at Central Iron and Steel Research Institute successively as assistant research scientist, associate professor, and professor in materials. He is assistant dean of Central Iron and Steel Research Institute. For over 20 years, Prof. Zhao has been mainly engaged in research on the atom or electronic structure and hydrogen storage materials. He received the outstanding contributions of young scientists by the National Natural Science Foundation of China in 1995, and a national special government allowance in 2006. His prizes include the Beijing outstanding young engineer in 2003 and the national defense science and technology innovation team, as an innovative team leader in 2008.